Modelling of metal anisotropy using the VPSC approach as UMAT within LS-DYNA

Leo Schwarzmeier[1], Nikolaus P. Papenberg[1], Alois C. Ott[1] and Johannes Kronsteiner[1]

[1]LKR Leichtmetallkompetenzzentrum Ranshofen GmbH, Austrian Institute of Technology, Lamprechtshausener Straße 61, 5258 Braunau am Inn/Ranshofen, Austria

Directional deformation processes like rolling and extrusion cause anisotropic mechanical properties due to reoriented crystallographic grains (texture). This anisotropy significantly affects processes like deep drawing. While numerical simulations can account for texture-dependent defects in forming simulations, many FE methods neglect evolving anisotropy or use fixed textures. Often this is the case because full-field crystal-plasticity (CP) FE models are computationally too demanding for industrial-relevant part sizes. This presentation shows the use of the visco-plastic self-consistent (VPSC) model as an efficient way of modelling a metal's developing texture and mechanical response. Coupling VPSC with LS-DYNA enables modelling developing texture in large-scale metal forming.

1 Introduction

Directional forming processes lead to the development of textures via crystallographic reorientation of grains. Due to the influence of developing texture on process chains, e.g. extrusion followed by rolling and forming, a metals initial microstructure and pre-deformation configuration has to be considered for more accurate simulations. Many finite element (FE) models have been created without considering evolving anisotropy or use fixed textures (e.g. Barlat [1], Cazacu [2], Kuwabara [3]). The reason is that full-field crystal-plasticity (CP) implementations in finite element frameworks (CPFE) [4] are computationally very demanding for industrial-relevant part sizes. This is because full-field CP models consider interactions between all individual crystals [5, 6]. Typically, CPFE is applied in the context of representative volume elements (RVEs), as done by Asgharzadeh et al. [7], leading to a typically rather low numerical efficiency. Wang et al. [8] reported good agreement with experiments using a CPFE model for the earing profiles during cup drawing of aluminium alloy (AA) 6K21, when comparing to conventional yield functions (Drucker, Hill48, YLD91). However, even when using only one solid element for modelling the metal thickness, the numerical effort of the CPFE model was still apprx. 13 times higher than that of the constitutive models in explicit LS-DYNA®.

Another approach to tackle the problem of expensive multi-scale simulations of deformation processes, is the use of meso-scale material models, which was applied in this work. We implemented the Visco-Plastic Self-Consistent (VPSC) [9] within a custom user defined material model (UMAT) in LS-DYNA® [10, 11].

This work shows how the influence of the evolving texture can be efficiently modelled by coupling the FE solver with VPSC (FE-VPSC). The approach is demonstrated for a part-scale metal forming application based on a puncture test, where texture and mechanical response is calculated by the VPSC-based material model for an AA 6082-T4 sheet metal. The simulation was compared to experimental results, with a contrast provided by a simulation of the same puncture test using a standard isotropic plasticity model.

2 Modelling Framework and Theory

The VPSC code of Lebensohn et al. [12] is based on the principles the of Visco-Plastic Self-Consistent theory by Molinari et al. [13]. In the underlying assumption, VPSC treats each grain as an ellipsoid inhomogenity inside a Homogeneous Effective Medium (HEM) [12, 14].

2.1 VPSC Polycrystal Relations between Grains

The continuum relation of Eq. (1) determines the connection between the viscoplastic strain rate tensor $\dot{\boldsymbol{\varepsilon}}_v$ at material point $\boldsymbol{x}$ of a continuum, connected to the location dependent deviatoric stress $\boldsymbol{\sigma}'$, the

© 2025 Copyright by Ansys Inc.

Schmid tensor $\boldsymbol{m}^s$ of the slip system s, each evaluated at a material point $\boldsymbol{x}$. N_s is the total number of available slip systems and $\bar{\tau}^s$ the corresponding threshold shear stress for slip system activation. n is a fitting parameter and the initial shear rate $\dot{\gamma}_0$, a normalization parameter. Note, Eq. (1) includes a sign factor as well, as the slip can happen in either positive or negative direction, which might be compensated by even numbers for n [15, 14]. The symbol ":" denotes double contracting indicies.

$$\dot{\boldsymbol{\varepsilon}}_v(\boldsymbol{x}) = \dot{\gamma}_0 \sum_{s=1}^{N_s} \boldsymbol{m}^s(\boldsymbol{x}) \left(\frac{|\boldsymbol{m}^s(\boldsymbol{x}) : \boldsymbol{\sigma}'(\boldsymbol{x})|}{\bar{\tau}^s(\boldsymbol{x})} \right)^n \times \text{sign}\left(\boldsymbol{m}^s(\boldsymbol{x}) : \boldsymbol{\sigma}'(\boldsymbol{x})\right) \tag{1}$$

The heart of the VPSC formulation is the self consistent linearization scheme, connecting the viscoplastic relation of the single crystals in the HEM with the properties of the polycrystal. There, each grain has an assigned orientation and a weight, and is treated as a ellipsoid inhomogeneity embedded in the HEM [12, 14]. Various linearization options, such as "tangent", "N-effective" or "secant", among others, are available in the VPSC implementation. Their mathematical details have been outlined in Tomé and Lebensohn [14] or Lebensohn et al. [16] in length. Seguardo et al. [15] note that results can differ substantially, depending on the option used. Improved VPSC versions, using the second order (SO) linearization approach, allow to calculate grain fragmentation as well as static and dynamic recrystallization as discussed by [17, 18, 19] and others.

In the presented results we have used the extended Voce hardening law to model the microscopic work hardening for the individual grains of the HEM. The Voce hardening law directly gives the critical resolved shear stress (CRSS) $\hat{\tau}^s$ of a slip system s by

$$\hat{\tau}^s = \tau_0^s + \left(\tau_1^s + \Theta_1^s \Gamma\right)\left[1 - \exp\left(-\Gamma \left|\frac{\Theta_0^s}{\tau_1^s}\right|\right)\right]. \tag{2}$$

In Eq. (2), $\Gamma = \sum_s |\gamma^s|$ is the accumulated total shear in the grain over all slip systems, τ_0^s is the initial threshold stress, Θ_0^s is the initial-, Θ_1^s the asymptotic hardening-rate and $\tau_0^s + \tau_1^s$ is the back-extrapolated flow stress [14].

Considering the possibility of self and latent hardening, a coupling coefficient $h^{s,s'}$ empirically accounts for the obstacles that the dislocations in a slip system s' pose to the ones in slip system s [14]. The increase of the threshold stress $\Delta\bar{\tau}^s$, due to shear activity $\Delta\gamma^{s'}$, can be calculated incrementally by

$$\Delta\bar{\tau}^s := \frac{\mathrm{d}\hat{\tau}^s}{\mathrm{d}\Gamma} \sum_{s'} h^{s,s'} |\Delta\gamma^{s'}|. \tag{3}$$

It is important to note that due to the local position of the grains being neglected in VPSC, the geometry of the polycrystalline aggregate is not regarded. This issue was adressed by Segurado et al. [15], where VPSC was first adapted to be a user defined material model (UMAT) for the FE solver ABAQUS®. Continuing work by Knezevic and Zecevic in [9, 20] expanded said UMAT into a generalized material model.

© 2025 Copyright by Ansys Inc.

2.2 Implementation of the VPSC model within LS-DYNA

We adapted the FE-VPSC version by Zecevic et al. [9] for use in LS-DYNA®. A custom interface converts the values of the microstructural calculations of FE-VPSC into an LS-DYNA® UMAT compatible format. The schematic in Fig. 1 illustrates the dependencies between the VPSC model used as an UMAT within the FE framework of LS-DYNA®. VPSC polycrystals are defined in a localized coordinate system in each FE integration point [15], of which we use one per finite element.

In each time step and for each element, the deformation increment and the current texture are passed to VPSC, which returns the stress response and updates the local texture [11]. The strain-induced work hardening of the HEM is considered by applying the Voce model of Eq. (2) for all grains of each integration point, using all enabled slip systems of the material. The implementation thereby accounts for the grain orientations and slip systems with respect to the local loading direction relevant for each element [11]. Fig. 1 further clarifies that the FE-VPSC approach requires micro-structural as well as macro-structural material information. The FE solver settings, refer to typical LS-DYNA® keyword files for the thermal / mechanical input, including FE-boundary conditions, FE solver criteria, part definitions and so on. For the local microstructure, the input refers to the polycrystalline information for VPSC, such as the available slip systems for deformation with their corresponding hardening parameters and the initial texture data provided as a list of orientations and their corresponding weights [14]. The evolving texture in each integration point is cached between the time steps and updated via the VPSC scheme. This approach allows the texture to evolve at points of different loading, even though all elements start at the same initial texture at the beginning of the process.

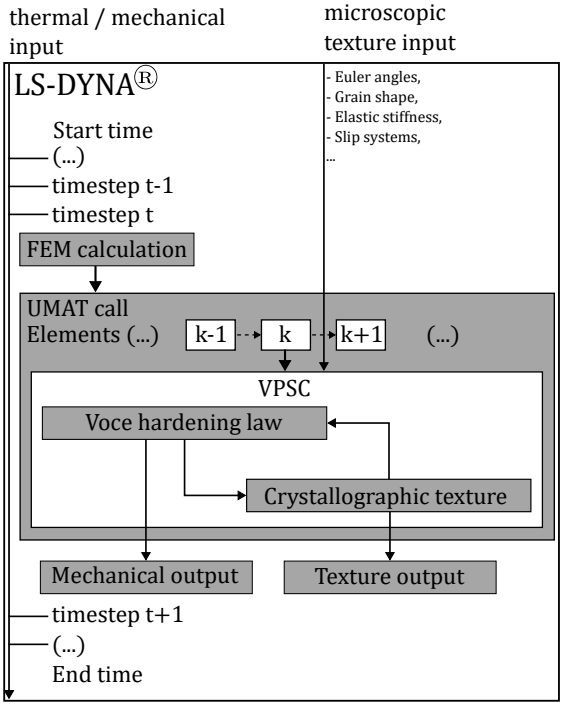

Figure 1: FE-VPSC as UMAT with Voce hardening law inside the macroscopic FE simulation [21].

3 Experimental Design

The material used in the experiments is industrially produced, 1.2 mm thick AA 6016-T4 rolled sheet metal. The mechanical behavior was analyzed via tensile testing and puncture tests, the texture was investigated via Electron Back-Scatter Diffraction (EBSD). To simulate the puncture tests, the material model was first calibrated using simulated tensile tests within the LS-OPT® framework to ensure accurate representation of the material's plastic behaviour within VPSC. Following parameter identification, numerical simulations of puncture tests were carried out using LS-DYNA®.

Two material models were employed for comparison in the LS-DYNA® simulation: (i) The physically motivated mean-field model (FE-VPSC) implemented via a user-defined material subroutine (UMAT), which incorporated the optimized Voce parameters. (ii) An isotropic, piecewise linear plasticity model based on the flow curve of AA 6016-T4, which was used as reference. The later model enabled comparative analysis of strain distributions during puncture loading, when disregarding texture information.

3.1 Deformation Experiments Setup

To determine the ductility of the metal sheet in the different process directions, uniaxial tensile tests were conducted in the Rolling Direction (RD), the Transverse Direction (TD) as well as at a 45° off-direction between RD and TD, on a multi purpose 4a Engineering Linovis testing machine. Fig. 2 shows the Linovis test chamber setup used for tensile testing. Labeled is the position of the FASTCAM NOVA S6

© 2025 Copyright by Ansys Inc.

high-speed camera for Digital Image Correlation (DIC) measurements. The tensile specimen is centrally positioned within the setup. The shown mirror is integrated into the configuration to direct the optical path from the camera to the specimen. DIC evaluation was accomplished via the MercuryRT v3.1 DIC-software. If DIC images are taken, a speckle pattern has to be applied to the sample beforehand. The modularity of the Linovis testing chamber allows the same system to be used for different mechanical testing procedures. For the puncture tests, the setup is modified by inserting a support, an impactor, and a blank-holder in place of the tensile specimen. In this configuration, the camera is aligned to capture the specimen head-on of the metal indention, ensuring accurate tracking of surface deformations in the TD, RD-plane during the test. Both, the tensile and the puncture tests, were displacement controlled and done at a constant velocity of 0.1 mm/s at Room Temperature (RT).

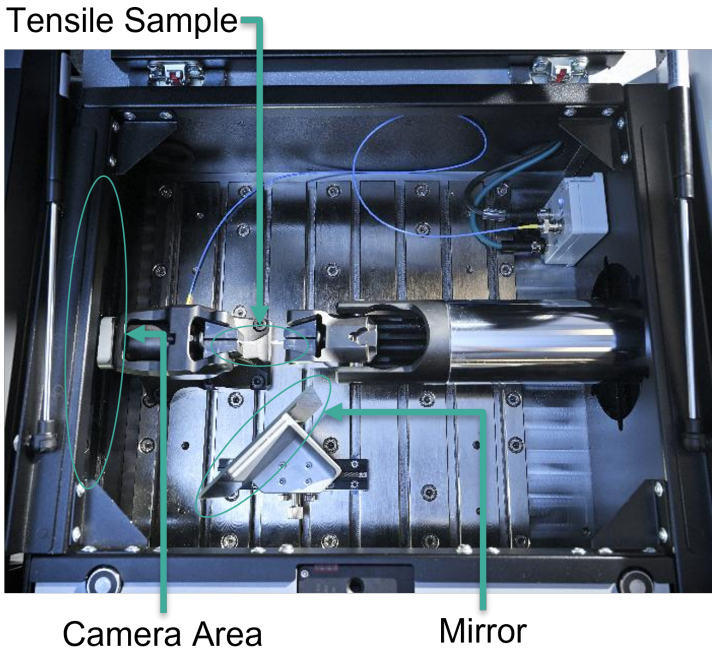

Figure 2: Testing chamber of Linovis machine with marked components. Setup for DIC on tensile tests specimen.

3.2 Microstructural Measurements

EBSD measurements were performed using a Tescan Mira 3 field emission scanning electron microscope. The measurements were conducted at an acceleration voltage of 20 kV, a working distance of 20 mm and a view field of 972 µm × 742 µm. Fig. 3a displays an Inverse Pole Figure (IPF) map of the measured texture, with the Normal Direction (ND), Transversal Direction (TD) and Rolling Direction (RD) of the sheet marked accordingly. For the pre-processing of input data, an alignment algorithm [22] was applied to correct for sample misalignment. A Pole Figure (PF) plot of the aligned texture data can be seen in Fig. 3b. Subsequently, the same clustering technique as used in [10, 11, 23] was employed to reduce the input data set, resulting in the identification of 70 representative grains. Note each pole in the PF of Fig. 3c has a individual weight assigned to it. For demonstration purposes, we used the largest cluster as input for the simulation, increasing the texture intensity and enforcing an anisotropic material behavior. The chosen input data corresponds to the initial crystallographic texture which is assigned to each integration point of the UMAT within the FE simulation.

© 2025 Copyright by Ansys Inc.

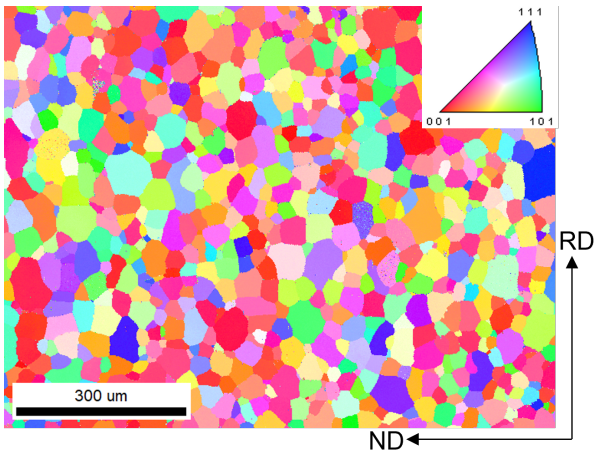

(a) IPF-map of rolled AA 6016-T4, Inlay shows coloring.

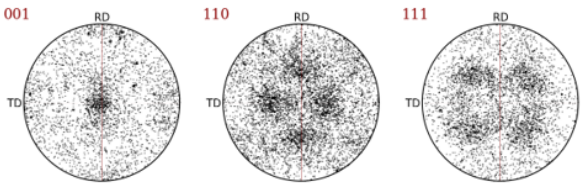

(b) PF of original, aligned texture

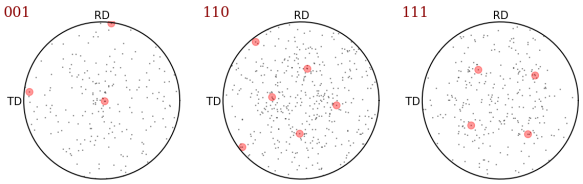

(c) PF of reduced reduced texture and largest cluster (red)

Figure 3: EBSD measurement of initial microstructure from an undeformed AA 6016-T4 sheet metal sample showing, (a) Inverse Pole Figure map, (b) aligned polefigures and (c) reduced polefigures.

3.3 Simulation Setup

Before performing computationally expensive deformation simulations in LS-DYNA®, the self-hardening parameters for VPSC must first be determined. For this purpose, the flow curve from an experimental tensile test along the RD is fitted via the software LS-OPT® v. 7.0.2, and the resulting parameters τ_0, τ_1, Θ_0 and Θ_1 of Eq. (2) for the $\{1\,1\,1\}\langle 1\,1\,0\rangle$ slip mode are subsequently used in puncture simulations. In both cases, VPSC employs the "N-effective" linearization with an interaction parameter of $n_{\text{eff}} = 10$.

3.3.1 Tensile Test Simulations

The geometry of a tensile specimen used for the determination of hardening parameters within an LS-OPT® optimization framework is shown in Fig. 4.

The tensile specimen features an overall length of 80 mm, with a length of 30 mm for a reduced central section measuring 10 mm in width. The transition between the wide and narrow sections is defined by a curvature radius of 20 mm. This region is the only meshed part of the specimen as it is critical for capturing the material response under tensile loading conditions. FE-VPSC was used as an UMAT in each element with the initial input texture of Fig. 3c. The upper and the lower part of the reduced section are pinned firmly in place by the tensile test machine which is reflected by corresponding boundary sets on the lower and upper nodes of the mesh. The tensile test is conducted under displacement control at a constant velocity of 0.1 mm/s in RD, enabling the calibration of hardening parameters of the UMAT, based on the observed mechanical response.

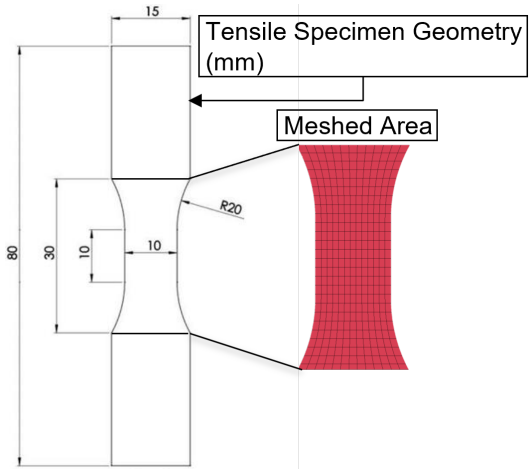

Figure 4: Measurements of tensile specimen. Only the free standing part has been meshed as clamps are modelled with corresponding fixed boundary conditions.

© 2025 Copyright by Ansys Inc.

3.3.2 Puncture Test Simulations

For experimental comparison of the distribution of the strain tensor components and displacement field, the AA 6016-T4 aluminium sheet with nominal dimensions of 80.0 mm × 80.0 mm × 1.2 mm was subjected to puncture loading. For the numerical simulation, the sheet metal was discretized using approximately 4.4k elements. The impactor, with a diameter of 20 mm, and the supporting fixture, featuring a hole of 40 mm in diameter, were modelled as rigid bodies. Contact interactions between aluminium and steel were incorporated to reflect the experimental setup. The impactor was driven by a displacement boundary condition, calibrated to match the constant velocity of 0.1 mm/s, as applied in the experiments. The steel blank-holder, present in the experimental setup, was not explicitly represented in the simulation. Instead, its mechanical constraint was approximated by applying fixed boundary conditions to selected nodes. Fig. 5 shows the described setup for the puncture test. The impactor moved along the Z-direction, which corresponds to the Normal Direction (ND) of the sheet. The metal sheet itself lies on the support in the XY-plane, i.e. along the Transversal Direction (TD) and Rolling Direction (RD).

A constant time increment of 1 s was employed throughout the simulation to ensure numerical stability and temporal resolution.

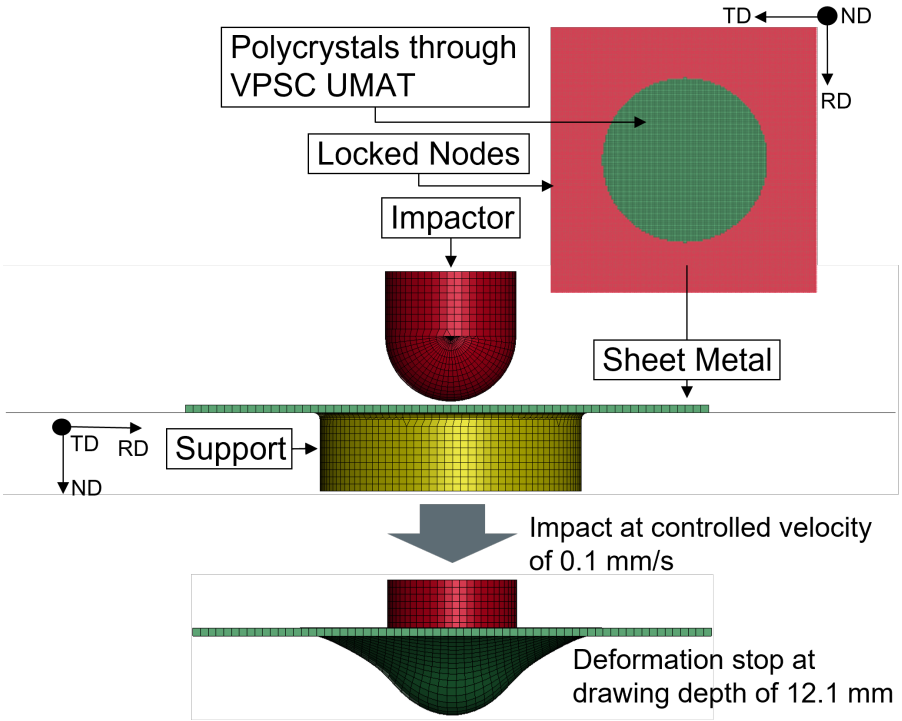

Figure 5: Overview of metal sheet sample, boundary conditions and puncture test setup.

Two such puncture test simulations were performed. One used the FE-VPSC UMAT for the metal sheet with the initial texture of Fig. 3c and the in Section 3.3.1 determined Voce hardening parameters, while the other used a standard piecewise linear plasticity model.

4 Results and Discussion

In Section 4.1 we explain the workflow for the determination of the fitted data for the tensile test, needed to evaluate the microscopic hardening values of the FCC slip mode. The fitted Voce values were afterwards used in the FE-VPSC puncture test simulations shown in Section 4.2.

© 2025 Copyright by Ansys Inc.

4.1 Simulating tensile tests for microstructural Hardening Values

The Voce hardening parameters were optimized using the corresponding force displacement curve. This calibration was performed within an LS-OPT® framework to ensure accurate representation of the material's plastic behaviour within VPSC. Fig. 6a displays the complete measured tensile load in RD, TD and 45° direction. The total displacement refers to the movement of the tool clamp. The plot in Fig 6b shows the best fitted load curve onto the measured force-displacement curve of the tensile sample in RD direction, which was used as a reference for the optimization until the Ultimate Tensile Strength (UTS) was reached. The LS-OPT® fitting framework used 3 iterations of 8 tensile simulations, testing different sets of hardening parameters $(\tau_0, \tau_1, \Theta_0, \Theta_1)$, sampled via a linear meta model and optimized towards a best fit using the Leapfrog Optimizer for Constrained minimization (LFOPC) approach [24].

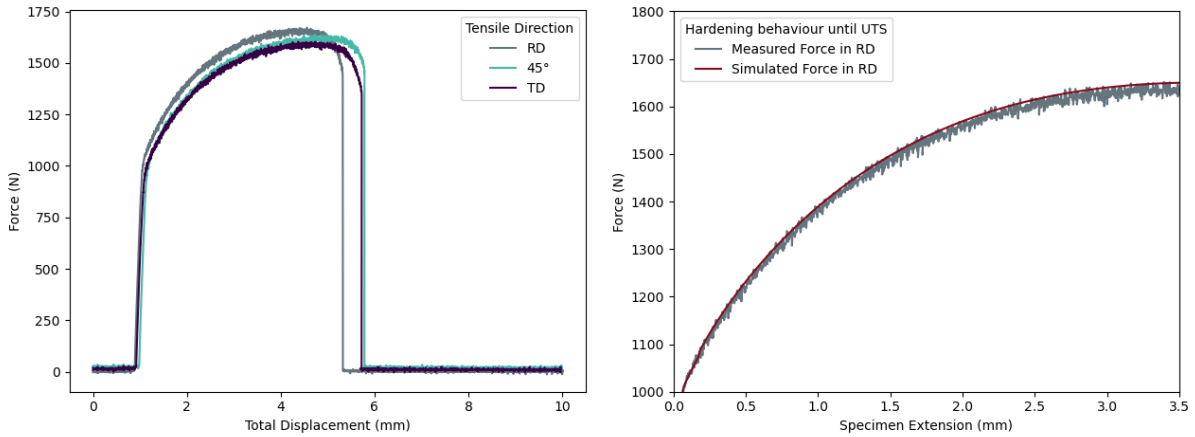

(a) Measured tensile forces in RD, TD and 45° direction against total tool displacement.

(b) Measured force per specimen elongation in RD and comparison to best fitting simulation.

Figure 6: Force-displacement curves of 1.2 mm *thick AA 6016-T4 sheet metal sample at room temperature.*

The Voce hardening law values for the best fit (Fig. 6b) were determined to be 66.18 MPa for τ_0^s, 68.56 MPa for τ_1^s, 423.28 MPa for θ_0^s, with a disabled stage IV hardening by setting θ_1^s to 0.00 MPa. Note, latent hardening was disregarded by setting the corresponding coefficient $h^{s,s'}$ in Eq. 3 to 1.

4.2 Puncture Test

Digital Image Correlation (DIC) taken from the puncture test metal sheet shortly before rupture is shown in Fig. 7. As mentioned in Section 3, the camera faced the impactor head-on, giving a plain view of the X,Y (RD,TD)-plane around the puncture area of the sheet metal. The asymetrical evolution of the strain components can either be caused by the inherent material anisotropy or test setup. While not shown here, the rupture of the sheets was found to occur solely parallel to the TD direction of the sheet.

© 2025 Copyright by Ansys Inc.

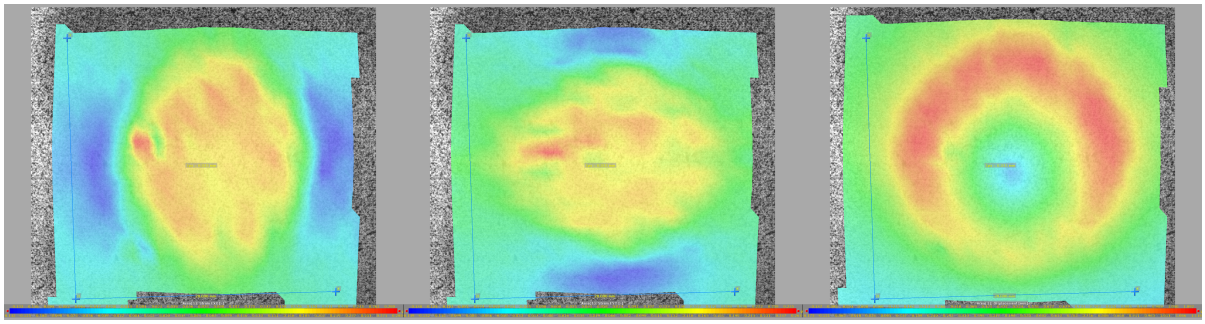

(a) X-Strain components in RD *(b) Y-Strain components in TD* *(c) Displacements in X,Y (TD,RD)*

Figure 7: DIC measurements of AA 6016-T4 metal sheet dent shortly before rupture occurrence. Each pixel (px) refers to 0.035 mm*. The blue X,Y-axes refer to RD,TD respectively, with the lengths reflecting* 20 mm*.*

The results from the simulations of the puncture tests using the FE-VPSC UMAT are shown in Fig. 8. The strain tensor and the displacement field components can be directly compared to DIC measurements in Fig. 7, which shows comparable behavior. The influence of the anisotropic behaviour is more distinct in the simulation for X and Y strains (Fig. 8a, 8b). This is not surprising, as only one cluster, accounting for a fraction of 6.6 %, was used for this work, thereby increasing the texture intensity and highlighting its influence on simulation and testing.

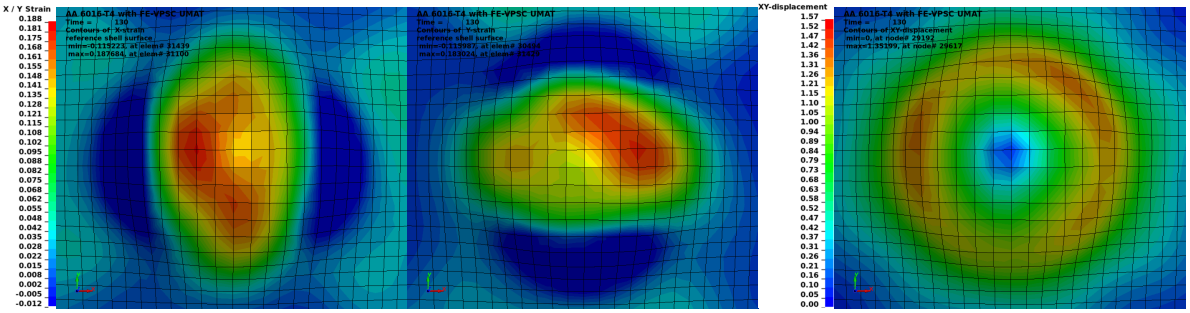

(a) X-Strain components in RD *(b) Y-Strain components in TD* *(c) Displacements in X,Y (TD,RD)*

Figure 8: X,Y strain/displacement distribution around dent of LS-DYNA® puncture test simulation using the FE-VPSC UMAT. Colorbars for the X,Y strain components plots (a,b) and the XY-displacement field (c) are respectively provided next to each.

The results using an isotropic material model are depicted in Fig. 9. The simulation is distinctively different from the experimental measurements (Fig. 7), showing no asymmetric distribution of strain.

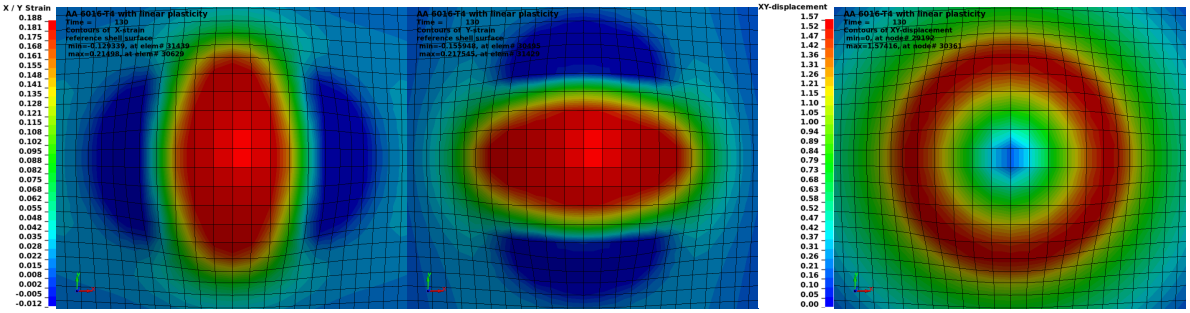

(a) X-Strain components in RD *(b) Y-Strain components in TD* *(c) Displacements in X,Y (TD,RD)*

Figure 9: X,Y strain/displacement distribution around dent of LS-DYNA® puncture test simulation using standard isotropic plasticity of an AA 6016-T4 flow curve. Colorbars for the X,Y strain components plots (a,b) and the XY-displacement field (c) are respectively provided next to each.

© 2025 Copyright by Ansys Inc.

Displayed in Fig. 10, a cross section of the metal sheet at the last simulated time step shows the differing deformation, when comparing the FE-VPSC model with the isotropic one. The contour plot of the effective strains highlights, how the deformation change is the result of the differently distributed strains over the sample geometry: Investigating the maximum strains, it becomes apparent that in the isotropic model of Fig. 10b, the maximum strains are larger and much more symmetrically localized, compared to the FE-VPSC model of Fig. 10a. The thinnest part of the punctured area in the simulation using the isotropic model has about 6 % less thickness compared to the thinnest part in the FE-VPSC model.

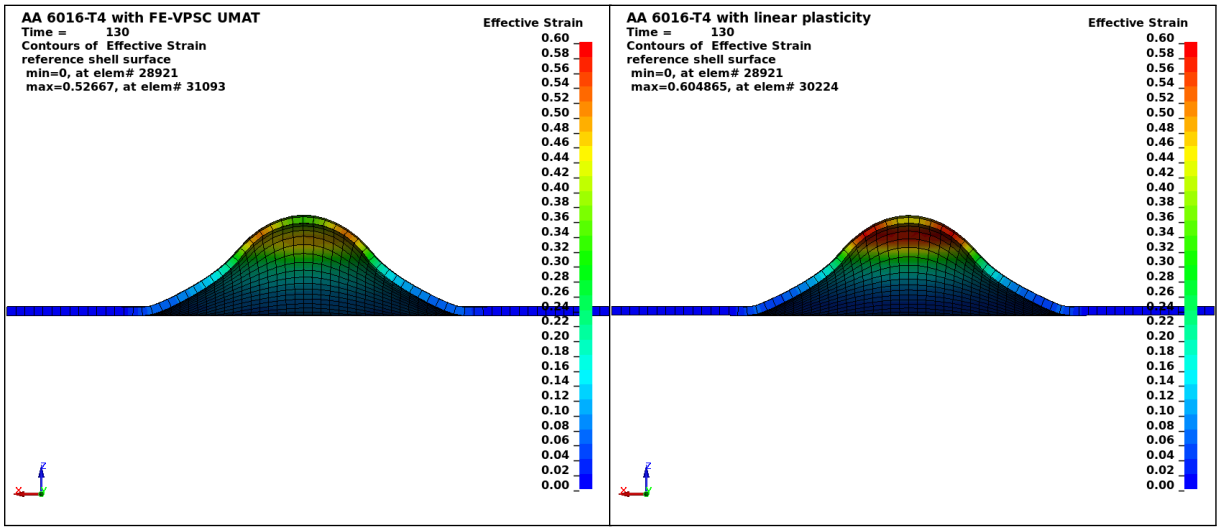

(a) Effective strain FE-VPSC *(b) Effective strain piecewise linear plasticity model*

Figure 10: TD,ND plane cross section of metal sheet (AA 6016-T4), showing different deformation due to different strains taking effect. X,Y,Z correspond to RD,TD,ND.

To provide an indication of the additional computation effort required for the microstructural simulation, the calculation times are given in the following. For the puncture test simulations conducted using FE-VPSC, the total CPU time required was 2 h, 21 min, and 35 s. In comparison, the simulation employing the isotropic material model completed in 16 min and 3 s. Both simulations used 8 nodes on our HPE Blade Cluster with Rocky Linux 8. Each node consisted of 16 × Intel® Xeon® E5-2667 v4, with 132 GB RAM.

5 Summary

In conclusion, this work has shown FE-VPSC coupled with LS-DYNA® as a useful method to simulate real world metal forming processes at multiple length scales, allowing to model and verify test setups, as well as more complex deformations. However, for the experimental comparison of the puncture test, variations in the tool setup can also have a major impact in the results and have to be investigated in future work. Still, FE-VPSC gives enables simulating process chains that include large deformation processes with evolving microstructure at each step, in the near future.

Authorship: **LS:** Writing - Original Draft, Simulations **NP:** Review & Editing, Validation, **ACO:** Data Curation, Experimental Design & Review, **JK:** Review & Supervision

Acknowledgements: The authors were supported by the project “Data-T-Rex” (Wi-2021-305676/13-Au) which is cofinanced by research subsidies granted by the government of Upper Austria. Thanks goes to the Los Alamos National Laboratory and especially Micoslav Zecevic for providing the FE-VPSC code.

© 2025 Copyright by Ansys Inc.

6 Literature

[1] Frédéric Barlat, Daniel J. Lege, and John C. Brem. “A six-component yield function for anisotropic materials”. In: Int. J. Plast. 7.7 (Jan. 1991), pp. 693–712. issn: 0749-6419. doi: 10.1016/0749-6419(91)90052-z.

[2] Oana Cazacu, Brian Plunkett, and Frédéric Barlat. “Orthotropic yield criterion for hexagonal closed packed metals”. In: Int. J. Plast. 22.7 (July 2006), pp. 1171–1194. issn: 0749-6419. doi: 10.1016/j.ijplas.2005.06.001.

[3] Toshihiko Kuwabara and Frédéric Barlat. “Deformation Behavior of Aluminum Alloys under Various Stress States: Material Modeling and Testing”. In: MATERIALS TRANSACTIONS 65.10 (Oct. 2024), pp. 1193–1217. issn: 1347-5320. doi: 10.2320/matertrans.mt-l2024010.

[4] F. Roters et al. “Overview of constitutive laws, kinematics, homogenization and multiscale methods in crystal plasticity finite-element modeling: Theory, experiments, applications”. In: Acta Mater. 58.4 (Feb. 2010), pp. 1152–1211. issn: 1359-6454. doi: 10.1016/j.actamat.2009.10.058.

[5] Marko Knezevic et al. “Three dimensional predictions of grain scale plasticity and grain boundaries using crystal plasticity finite element models”. In: Comput. Method. Appl. Mech. Eng. 277 (Aug. 2014), pp. 239–259. issn: 0045-7825. doi: 10.1016/j.cma.2014.05.003.

[6] D.A. Ruiz Sarrazola, D. Pino Muñoz, and M. Bernacki. “A new numerical framework for the full field modeling of dynamic recrystallization in a CPFEM context”. In: Comp. Mat. Sci. 179 (June 2020), p. 109645. issn: 0927-0256. doi: 10.1016/j.commatsci.2020.109645.

[7] Amir Asgharzadeh et al. “A Computationally Efficient Multiscale, Multi-Phase Modeling Approach Based on CPFEM to Assess the Effect of Second Phase Particles on Mechanical Properties”. In: Crystals 13.8 (Aug. 2023), p. 1199. issn: 2073-4352. doi: 10.3390/cryst13081199.

[8] Songchen Wang et al. “Multi-scale numerical investigation of deep drawing of 6K21 aluminum alloy by crystal plasticity and a stress-invariant based anisotropic yield function under non-associated flow rule”. In: J. Manuf. Proc. 102 (Sept. 2023), pp. 736–755. issn: 1526-6125. doi: 10.1016/j.jmapro.2023.07.067.

[9] Miroslav Zecevic and Marko Knezevic. “A new visco-plastic self-consistent formulation implicit in dislocation-based hardening within implicit finite elements: Application to high strain rate and impact deformation of tantalum”. In: Comput. Method. Appl. Mech. Eng. 341 (Nov. 2018), pp. 888–916. issn: 0045-7825. doi: 10.1016/j.cma.2018.07.027.

[10] Johannes Kronsteiner et al. “Modeling of Texture Development during Metal Forming Using Finite Element Visco-Plastic Self-Consistent Model”. In: Crystals 14.6 (June 2024), p. 533. issn: 2073-4352. doi: 10.3390/cryst14060533.

[11] J. Kronsteiner et al. “Integrating texture evolution into a deep-drawing simulation via viscoplastic self-consistent model”. In: Materials Characterization 224 (June 2025), p. 114970. issn: 1044-5803. doi: 10.1016/j.matchar.2025.114970.

[12] R.A. Lebensohn and N. Tomé C. “A self-consistent anisotropic approach for the simulation of plastic deformation and texture development of polycrystals: Application to zirconium alloys”. In: Acta Metall. Mater. 41.9 (Sept. 1993), pp. 2611–2624. issn: 0956-7151. doi: 10.1016/0956-7151(93)90130-k.

[13] A. Molinari, G.R. Canova, and S. Ahzi. “A self consistent approach of the large deformation polycrystal viscoplasticity”. In: Acta Metallurgica 35.12 (Dec. 1987), pp. 2983–2994. issn: 0001-6160. doi: 10.1016/0001-6160(87)90297-5.

[14] Carlos N. Tomé. Material Modeling with the Visco-Plastic Self-Consistent (VPSC) Approach. Ed. by Ricardo A. Lebensohn. Elsevier Series on Plasticity of Materials Series. San Diego: Elsevier, 2023. 1381 pp. isbn: 9780128207208. doi: 10.1016/C2019-0-01217-4.

[15] Javier Segurado et al. “Multiscale modeling of plasticity based on embedding the viscoplastic self-consistent formulation in implicit finite elements”. In: Int. J. Plast. 28.1 (Jan. 2012), pp. 124–140. issn: 0749-6419. doi: 10.1016/j.ijplas.2011.07.002.

© 2025 Copyright by Ansys Inc.

[16] Ricardo A. Lebensohn, C. N. Tomé, and P. Ponte CastaÑeda. “Self-consistent modelling of the mechanical behaviour of viscoplastic polycrystals incorporating intragranular field fluctuations”. In: Philosophical Magazine 87.28 (Aug. 2007), pp. 4287–4322. issn: 1478-6443. doi: 10.1080/14786430701432619.

[17] Miroslav Zecevic et al. “Modeling of intragranular misorientation and grain fragmentation in polycrystalline materials using the viscoplastic self-consistent formulation”. In: International Journal of Plasticity 109 (Oct. 2018), pp. 193–211. issn: 0749-6419. doi: 10.1016/j.ijplas.2018.06.004.

[18] Iftekhar A. Riyad and Marko Knezevic. “Field fluctuations viscoplastic self-consistent crystal plasticity: Applications to predicting texture evolution during deformation and recrystallization of cubic polycrystalline metals”. In: Acta Materialia 261 (Dec. 2023), p. 119395. issn: 1359-6454. doi: 10.1016/j.actamat.2023.119395.

[19] Iftekhar A. Riyad and Marko Knezevic. “Predicting the evolution of texture and grain size during deformation and recrystallization of polycrystals using field fluctuations viscoplastic self-consistent crystal plasticity”. In: Mechanics of Materials 200 (Jan. 2025), p. 105212. issn: 0167-6636. doi: 10.1016/j.mechmat.2024.105212.

[20] Miroslav Zecevic et al. “Viscoplastic self-consistent formulation as generalized material model for solid mechanics applications”. In: Appl. Eng. Sci. 6 (June 2021), p. 100040. issn: 2666-4968. doi: 10.1016/j.apples.2021.100040.

[21] Leo Schwarzmeier. “Introduction of multiple slip systems for anisotropic microstructure modelling in FEM-framework”. en. In: (2025). doi: 10.25365/THESIS.78459.

[22] Alois C Ott et al. “Automatic Texture Alignment by Optimization Method”. In: Microscopy and Microanalysis 30.2 (Mar. 2024), pp. 253–277. issn: 1435-8115. doi: 10.1093/mam/ozae013.

[23] Alois C. Ott et al. “Evaluation of a clustering algorithm for texture data”. In: Materials Characterization 225 (July 2025), p. 115122. issn: 1044-5803. doi: 10.1016/j.matchar.2025.115122.

[24] Nielen Stander et al. LS-OPT User’s Manual. Version 7.0. A DESIGN OPTIMIZATION ANDPROBABILISTIC ANALYSIS TOOLFOR THE ENGINEERING ANALYST. LSTC. Livermore, CA, Nov. 2020. url: https://www.lsoptsupport.com/documents/manuals/ls-opt/lsopt_70_manual.pdf.

© 2025 Copyright by Ansys Inc.